buildings

MDPI

Article

Study on Mechanical Properties of Steel Fiber-Reinforced Geopolymer Concrete under Multi-Axial Loads

Pengtao Wu [1,2,3], Xuan Wan [1], Qun Lu [1] and Yan Zhang [1,*]

[1] Tianjin Key Laboratory of Civil Structure Protection and Reinforcement, Tianjin Chengjian University, Tianjin 300384, China; wupengtao0228@tcu.edu.cn (P.W.); wxdyx19980108@163.com (X.W.); zdlq585@126.com (Q.L.)
[2] School of Civil Engineering, Tianjin University, Tianjin 300372, China
[3] Tianjin Building Materials Science Research Academy Co., Ltd., Tianjin 300381, China
* Correspondence: zy_801010@163.com

Abstract: Steel fiber-reinforced geopolymer concrete (SFRGPC) is an inorganic cementitious material with environmentally friendly features. As compared to conventional concrete, SFRGPC has greater strength and durability, but it is brittle, making it similar to ordinary concrete. To date, the triaxial mechanical properties that regulate SFRGPC's structural performance at serviceable and ultimate-limit conditions remain poorly understood. In this study, we conducted experimental and theoretical analyses of these properties. Conventional triaxial testing is used to investigate the effects of varying steel fiber contents and ratio of length to diameter under different confinement pressures on SFRGPC's mechanical properties. The failure mode, maximal strength, stress–strain curve, maximum strain, and compressive toughness were analyzed and discussed. Under uniaxial compression, the failure mode of the SFRGPC specimens was a longitudinal split failure. The brittleness of the SFRGPC can be eliminated, and its resistance to breaking can be greatly improved by increasing the volume of steel fibers and the confining pressure in the mixture. The steel fiber content and ratio of length to diameter have obvious influence on the compressive strength of SFRGPC. As the steel fiber content increased, the compressive strength increased by 1.15–1.44 times; as the ratio of length to diameter increased, the compressive strength increased by 1.21–1.70 times. The increase in confining pressure can improve the compressive strength of concrete. With the increase in confining pressure, the increase trend of compressive strength becomes smooth. The confining pressure, steel fiber content, and steel fiber length have substantial influences on the compressive toughness index η_{c3}. Under increasing confining pressure, η_{c3} increases linearly; however, after confining pressure is higher than 5 MPa, η_{c3} tends toward a steady state when the confining pressure increases. Using numerical simulation, we also investigated the size effect of SFRGPC under triaxial load. The concrete cylinder's strength does not significantly decrease as its size increases.

Keywords: steel fiber-reinforced geopolymer concrete; triaxial; mechanical properties; numerical simulation

Citation: Wu, P.; Wan, X.; Lu, Q.; Zhang, Y. Study on Mechanical Properties of Steel Fiber-Reinforced Geopolymer Concrete under Multi-Axial Loads. *Buildings* **2024**, *14*, 2780. https://doi.org/10.3390/buildings14092780

Academic Editors: Hsuan-Teh Hu and Grzegorz Ludwik Golewski

Received: 8 July 2024
Revised: 9 August 2024
Accepted: 30 August 2024
Published: 4 September 2024

1. Introduction

In recent decades, concrete materials have been more and more widely used in building structures; with the global climate change and the increasingly serious environmental pollution problems, resource reuse, to achieve the "double carbon" goal has become a common concept of global development. The development of renewable energy can not only reduce the consumption of limited energy resources but also effectively reduce the emission of air pollutants, improve environmental quality, and enhance people's quality of life. The mechanical properties of geopolymer concrete (GPC) have been studied by many scholars. For instance, in kaolin-rich regions, the price of geopolymer concrete is higher than that of traditional Portland cement, while the amount of greenhouse gas produced by the formation of geopolymers from kaolin is 40% less than that of conventional

cement [1–3]. In addition, some studies suggest that using a mixture of sodium hydroxide and sodium silicate as an alkali activator can significantly enhance GPC's properties as compared to using only NaOH [4,5]. It was investigated the durability and static properties of self-compacting geopolymer cementitious concrete made from fly ash, mineral particles, wollastonite, and graphene oxide [6]. Ghafoor et al. [7] studied the effects of two different Na_2SiO_3/NaOH ratios and the ratio of alkaline activator to fly ash (AA/FA) on the mechanical properties of solidified GPC using two locally produced fly ashes with different NaOH concentrations. Lincy et al. [8] added a small quantity of silica nanoparticles to an optimized GPC mixture to determine its additive impact on the performance of mixed GPC paver blocks.

At the early stage of the research, GPC was mixed without coarse aggregate. Although it had the advantages of high early strength and low carbon dioxide emission, its brittleness was particularly obvious. In addition, its tensile strength was low, so the application of GPC was limited [9]. Therefore, the method of fiber-reinforced concrete is used for reference, and various types of fibers are added to GPC to improve its bending strength and energy absorption capacity. The selection of fibers to use as reinforcement must take into account the following requirements [10]: (1) the compatibility between the material properties and the application; (2) a sufficient fiber–matrix interaction to transfer stress; and (3) an optimal length–diameter ratio to ensure effective post-cracking behavior.

With the addition of fibers to increase the strength and energy absorption capacity of GPC, many researchers began to focus on the use of various fibers to improve the mechanical properties of GPC. Ganesh [11] discovered that as the amount of glass fiber in GPC increased, the material's resistance and energy absorption capacity increased while its brittleness decreased substantially. Similarly, by measuring the physical and mechanical energies of steel fiber-reinforced geopolymer concrete (SFRGPC) [12], it was determined that the addition of fibers substantially enhanced the material's tensile strength. The structural energy of steel fiber and ceramic pellets as additives to GPC was investigated, indicating that the impact strength of the polymer can be considerably enhanced with these reinforcements [13]. Noushini [14] measured the mechanical and physical properties of polymer gel materials with various types of fibers, finding that polyolefin fiber fracturing was the most significant for the same volume of fiber. In other research, Liu et al. [15] discovered that an increase in fiber content can reduce the quantity of concrete and ease and that the fiber's ease decreases further with longer fibers. The smaller the fiber diameter and the longer the fiber, the stronger the concrete. Sharma et al. [16] concludes that the use of fiber-reinforced geopolymer concrete should be commercialized after the establishment of proper standards for manufacturing. The mechanical properties of fiber-reinforced geopolymer concretes were reviewed, and the development and application prospects of fiber-reinforced geopolymer concrete were introduced. Meskhi et al. [17] studied the application potential of geopolymer concrete in construction practice and evaluated it in detail. In order to improve the strength and durability of GPC and its sustainability, an optimal ratio of GPC based on glass fiber and waste basalt powder was proposed. Celik et al. [18] presented a comprehensive exploration of multiple parameters aimed at improving the strength, workability, setting time, and environmentally friendly properties of GPC. Özkılıç et al. [19] studied the influence of waste glass aggregate with fly ash in certain proportions by different amounts of molarity and waste glass aggregate proportion on GPC.

In practical engineering applications, engineering structures are often in a state of multi-axial complex load. Under multi-axial stress, the compressive strength, elastic modulus, and failure mode of concrete materials will change significantly. Therefore, it is neither reasonable nor reliable to guide engineering design only on the basis of the mechanical properties measured by uniaxial experiments.

Since the 1970s, a number of studies have concentrated on the triaxial properties of normal concrete (NC) [20], high-performance concrete (HPC), or the uniaxial properties of high-strength concrete or ultra-high-performance concrete (UHPC). Zhou et al. [21] ob-

served the tensile brittle failure mode of high-performance concrete (HPC) specimens under tensile–compressive–compressive (T-C-C) loading. They found that UHPC's triaxial compressive strength and ductility increase with confinement pressure [22]. In addition, their tests showed that the shear and expansion failure modes of UHPC are realized effectively, and the maximal axial strain increases linearly with the confining pressure. In relevant research, the failure of cylindrical specimens of UHPC was considerably delayed compared to ultra-high-strength concrete (UHSC) [23]. In contrast to fiber-reinforced geopolymer composite samples, Khan et al. [24] found that the confining pressure significantly affects the compressive strength of HSG materials. In another study, the constitutive relationships and failure criteria of entirely recycled concrete (TRC) under triaxial compression at high temperature were investigated [25]. Zhang et al. [26] experimentally and numerically investigated the triaxial mechanical behavior of a reactive powder cement slurry prepared with an alcohol-based shrinkage reducer.

In order to further study the strengthening properties of steel fiber on concrete materials, numerous researchers have explored the experimental triaxial compression performance of steel fiber-reinforced concrete (SFRC) [27–29] and found that with an increase in the confining pressure and fiber content, the compressive strength, tensile strength, Poisson's ratio, failure mode, and deformation of concrete are evidently altered. Wang et al. [30] systematically analyzed the effects of varying contents and confining pressures on the triaxial compressive strength of SFRC. Wang et al. [31] analyzed the triaxial strength and deformation characteristics of SFRC with different steel fiber volume ratios under three distinct strain powers and established a set of spatial failure criteria for SFRC. However, the triaxial mechanical properties of SFRGPC have been rarely studied.

Therefore, it is particularly important to study the triaxial mechanical properties and static constitutive relationships of ultra-high-performance concrete materials. Examining the mechanical properties of SFRGPC under uniaxial and multi-axial stress is necessary to derive accurate constitutive models. This study presents the results of uniaxial and triaxial compression tests conducted on SFRGPC and analyzes the mechanical behavior of SFRGPC under various stress conditions. The test results demonstrate the effects of confinement conditions on the compressive strength and ductility, stress–strain curves, and failure modes of SFRGPC. The specific application of SFRGPC in other practical scenarios is supported by test data. This research provides crucial mechanical parameters for the structural design of geopolymer concrete under complex stress conditions.

2. Experiments Program

2.1. Materials

To enhance the uniformity of the generated SFRGPC samples, this study employed the following material components: cementitious materials (slag powder, silica fume, fly ash, silica powder, the mixture ratio is 0.72:0.07:0.12:0.09), an alkaline activator (sodium silicate solution, sodium hydroxide), quartz sand, and steel fibers (Table 1, Figure 1), and superplasticizer. Table 2 shows the resulting mixture ratio that satisfied the requirements after experimenting with numerous mixtures. In addition, the table displays the composition of the SFRGPC used in the present study. To decrease the binder and internal porosities, improve the gradation of the geopolymer-based concrete aggregates, and increase compactness, we used three distinct steel filaments. Quartz sand can be used in geopolymer concrete to adjust the water–binder ratio, enhance the concrete's density and strength, and provide strong resistance against acid corrosion. These experiments tested fine (70–140 mesh), medium (50–70 mesh), and coarse (>70 mesh) ISO-standard quartz sands. The superplasticizer is a polycarboxylic acid superplasticizer with a solid content of 40%.

Unlike conventional HPC, quartz sand conforming to ISO standards was readily available. Additionally, ultrafine industrial waste powder, such as fly ash and mineral powder, was utilized to supplant a portion of the silica particles. As shown in Table 2, ultrafine industrial waste powder (silica fume, fly ash, silica powder, and mineral powder)

comprised approximately 44% of the binder, while the proportion of expensive silica fume was only 4%, and the water–binder ratio was 0.1. Since the production of cement and fine quartz sand requires more energy and resources and the output of silica fume is limited and more expensive than that of fly ash, silica powder, and mineral powder, the UHPC used in this test demonstrates energy and cost savings.

Steel fiber is a form of ultra-light, copper-based steel wire that is available in flat, hooked, wavy, and spiral configurations. It has a tensile strength exceeding 4000 MPa. Steel fiber can improve the tensile strength and deformation capacity of concrete, providing an optimal balance between workability and strong mechanical properties. The diameter of the steel fibers used in this experiment was 0.12 mm, and their lengths were 6, 10, and 15 mm.

Table 1. Mechanical properties of steel fibers.

Steel Fiber	Elastic Modulus (MPa)	Tensile Strength (MPa)	Diameter (mm)	Length (mm)	Aspect Ratio
MF06	2.1×10^5	4295	0.12	6	50
MF10	2.1×10^5	4295	0.12	10	83
MF15	2.1×10^5	4295	0.12	15	125

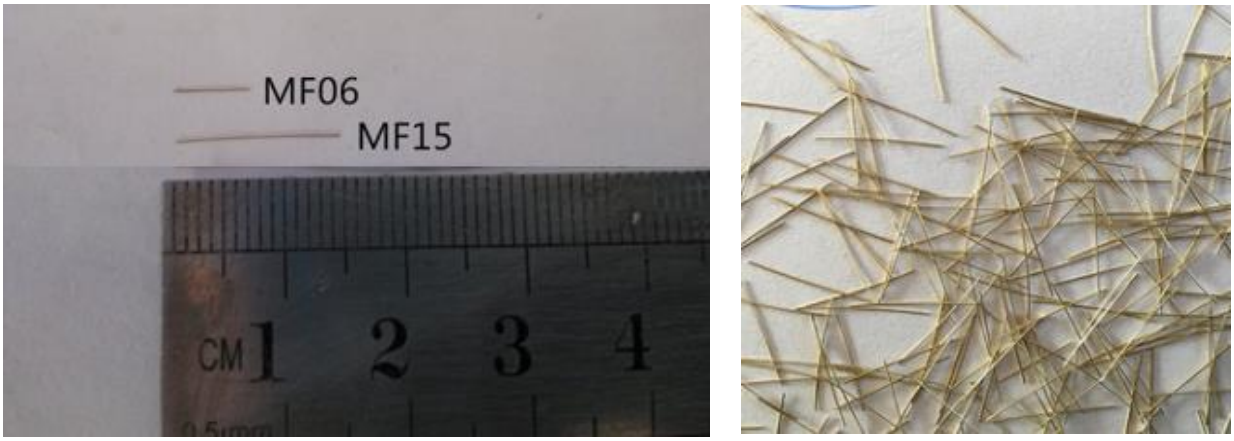

(**a**) 6 mm and 15 mm (**b**) 10 mm

Figure 1. Steel fiber.

Table 2. Mixture proportions of SFRGPC samples.

Group	Steel Fiber	Steel Fiber Volume Fraction V_f (%)	Cementitious (kg/m^3)	Quartz Sand (kg/m^3)	Basic Activator (kg/m^3)	Superplasticizer (kg/m^3)
S0	--	0	1292	950	699	9.8
S1	MF06	2.5	1292	950	699	9.8
S2	MF10	2.5	1292	950	699	9.8
S3	MF15	1.0	1292	950	699	9.8
S4	MF15	2.0	1292	950	699	9.8

2.2. Specimens

Silica fume, fly ash, mineral powder, quartz sand, and additional raw materials were added to a mixer and mixed for five minutes. After thoroughly combining the granular ingredients, we added a pre-blended solution of the alkaline stimulant, water, and water-reducing agent, followed by the addition of the steel fiber. After completely incorporating the steel fiber into the concrete, we continued mixing for three minutes. The specimens were cured at 20 °C and a relative humidity of greater than 95%. After 24 to 48 h, the sample was demolded and stored for 28 days in an indoor curing chamber. After curing, SFRGPC

specimens were extracted using an automatic coring machine, and their two planes were polished to meet the test requirements. To test with a uniform distribution of steel fibers, we took sections from the center of the rectangular specimens so that they accurately reflect the mechanical properties after curing. The final specimens are depicted in Figure 2. Each group consists of three specimens, the failure mode and stress–strain curve selected are the most representative.

(**a**) SFRGPC mixing (**b**) Compressive specimens

Figure 2. Specimens of SFRGPC for uniaxial and triaxial tests.

2.3. Experimental Setup

This experiment used an RMT-150C (The equipment was developed and produced by Wuhan Institute of Rock and Soil Mechanics, Chinese Academy of Sciences), a computer-controlled, three-axis, electro-hydraulic servo pressure testing device (Figure 3). The test is carried out according to the test standard recommended by the International Association of Rock Mechanics [32]. The RMT-150C's loading mechanism consists of two separate loading devices: (1) a hydraulic actuator with servo control that exerts an axial force of up to 1000 kN and (2) a high-pressure container that uses hydraulic oil to uniformly apply confining pressure to the whole sample surface. A constricting pressure of up to 50 MPa was applied to the specimen's surface. The specimen's axial deformation was measured using a linear variable differential transformer (LVDT). The average recorded deformation was used to represent the axial distortion.

Figure 3. RMT 150C system.

Figure 4 depicts the stress state of the sample under conventional triaxial compression. To measure uniaxial compression, we employed the displacement control method with a uniaxial loading rate of 0.02 mm/min.

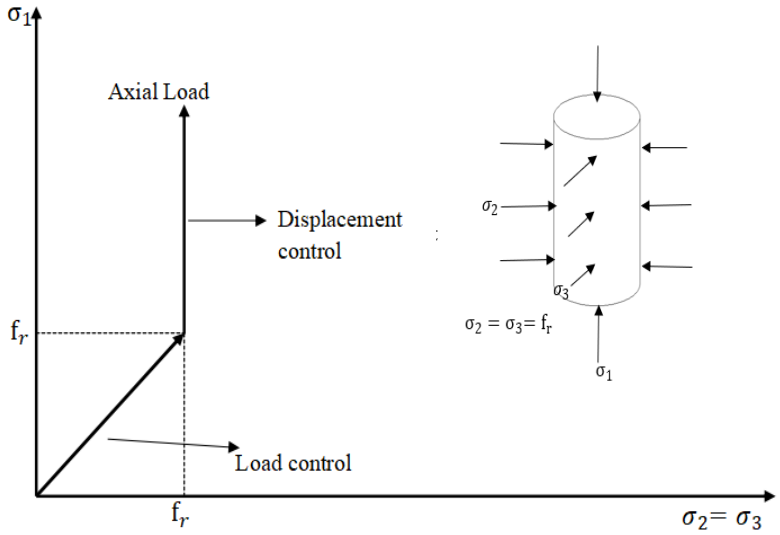

Figure 4. Development of stress in the triaxial compression test.

The confining pressure and axial load were simultaneously applied to the surface of the geopolymer concrete specimen ($\sigma_1 = \sigma_2 = \sigma_3$, σ_1, σ_2 and σ_3 correspond to the principal stresses of the X, Y, and Z axes, respectively) using the force control method to test the conventional triaxial compression. Figure 4 shows the stress state of the sample under conventional triaxial compression. After maintaining the confining pressure below the set value for 10 s to achieve a constant confining pressure, the axial loading rate was altered to 1 kN/s on the top surface of the SFRGPC specimen to apply axial stress up to 80% of the ultimate strength. The load was then administered using the displacement control method at a loading rate of 0.02 mm/min until failure. The tested confinement pressures ranged were 5, 10, 15, 20, 30, and 40 MPa.

3. Experimental Results

3.1. Failure Modes

Figure 5 describes the failure patterns of GPC under various confining pressure conditions. All fracture surfaces were relatively planar, with no bonding effects. At the outset of the uniaxial compression test, a vertical crack parallel to the loading direction appeared in the middle of the specimen. As the load increased, one or more fractures developed. The specimen's failure mode was a longitudinal split failure. Under axial load, the specimen was axially compressed, while the radial direction was subject to tension. With the increase in axial stress, the radial dimension expanded. When the tensile stress exceeded the ultimate tensile strength, tiny fractures began to develop in the specimens. As the stress increased, the cracks progressively expanded and lengthened, and a small amount of concrete spalling occurred. Eventually, the developed test specimen split obliquely through cracking, resulting in the specimen's destruction, which occurred when the confining pressure was between 5 and 20 MPa and the development direction of the oblique fracture was 60 to 70 degrees relative to the horizontal. As the confining pressure rose, the damage patterns became oblique rupture failures, and the angle of crack development tended to decrease marginally.

Figures 6–9 depict the failure patterns of the SFRGPC specimens under varying confining pressures. The addition of steel fibers substantially altered the failure modes of the specimens. After the addition of steel fiber, the integrity of the specimen improved, and the fractures occurring in the specimen were smaller. During the uniaxial compression test, the SFRGPC specimens were compressed axially and tensioned tangentially. As axial stress

increased, the radial expansion of the SFRGPC specimen commenced. When the tensile stress exceeded the ultimate tensile strength, micro-fractures appeared. In response to the increasing tension, the cracks grew and penetrated the specimen, which was ultimately destroyed. Because of the lateral restraint of the confining pressure and the bridging effect of the steel fiber, the test specimens expanded radially during the triaxial test. The specimens displayed oblique shear failure, and their fractures were relatively fine. The original integrity was largely preserved, and they did not fracture into two or more fragments like the specimens lacking steel fiber. Thus, the steel fiber increased the ductility of the GPC, allowing the specimen to absorb more energy during the failure process.

Figure 5. Failure patterns of GPC specimens under different confining pressure conditions.

Figure 6. Failure patterns of the SFRGPC specimens with 1.0% MF15.

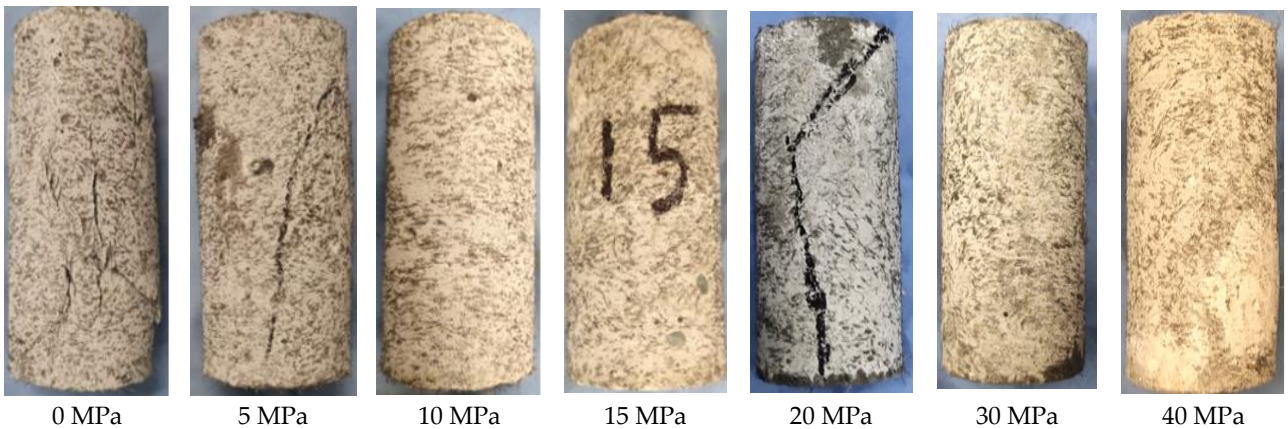

Figure 7. Failure patterns of the SFRGPC specimens with 2.0% MF15.

Figure 8. Failure patterns of the SFRGPC specimens with 2.5% MF06.

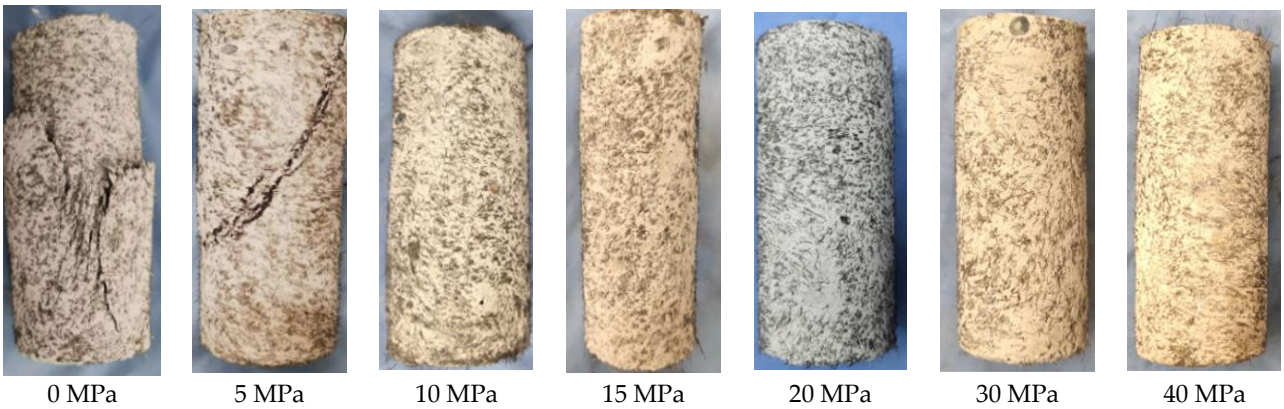

Figure 9. Failure patterns of the SFRGPC specimens with 2.5% MF10.

3.2. Stress–Strain Curves

Figure 10 depicts the complete axial stress–strain contours of the SFRGPC specimens subjected to various confining pressures. Figure 10a shows that the GPC exhibited a characteristic brittle failure curve when subjected to multi-axial compression. As the confining pressure increased, the strength and deformation of the GPC specimens increased by varying degrees, and the confining pressure limited the lateral deformation of specimens to some degree. Figure 10b–e illustrate that the peak stress and peak strain of the SFRGPC specimens increased substantially with the confining pressure. These outcomes indicate that the peak tension and peak strain increase with the increased addition of steel fiber content. Therefore, steel fiber can considerably improve the SFRGPC's strength and ductility. However, when the steel fiber exceeds a particular control content, the influence of the peak stress and peak strain decreases and stabilizes.

Analysis of the results reveals that the confining pressure had a greater effect on the tensile strength of the SFRGPC specimens. For specimens containing varying amounts of steel fiber, the triaxial compressive strength increased with the confining pressure. As the confining pressure increased, the specimens' lateral deformation was further constrained. The specimen was compressed further as the axial load increased, and the stress–strain curve exhibits an increasing trend. Consequently, the triaxial compression strength is represented by its first yield point, and the corresponding strain cannot be considered the maximum strain. The respective strain is not considered as the peak strain and is not enumerated in Table 3.

Without the addition of steel fiber, the respective increases in strength under various confining pressures of 5, 10, 15, 20, 30, and 40 MPa were 83%, 115%, 170%, 225%, 297%, and 374%. At an MF15 fiber volume ratio of 1.0%, the respective increments under various confining pressures were 95%, 144%, 233%, 308%, 349%, and 407%. The increments in

various confining pressures were 111%, 171%, 221%, 276%, 341%, and 421% when the MF15 fiber volume ratio increased to 2.0%. At an MF06 fiber volume ratio of 2.5%, the respective increases in confining pressure were 101%, 173%, 218%, 254%, 298%, and 371%. Further increasing the MF10 fiber volume ratio to 2.5% resulted in increases of 110.4%, 178%, 258%, 290%, 386%, and 507%, respectively.

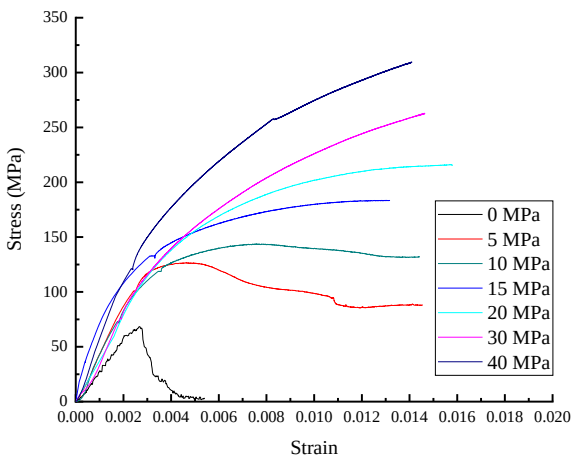

(**a**) Without steel fiber

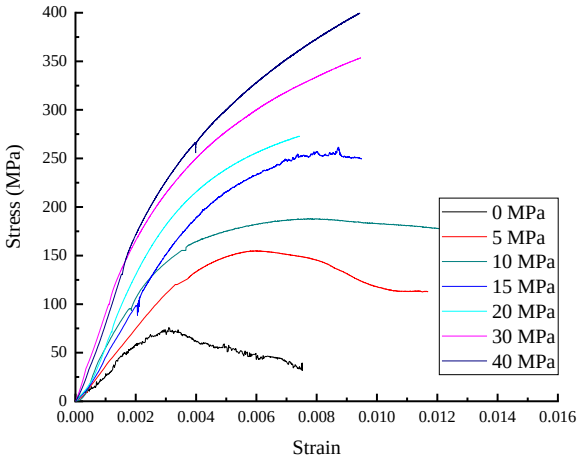

(**b**) 1.0% MF15

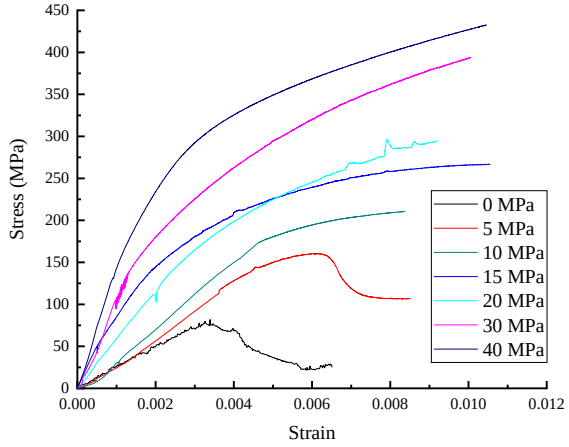

(**c**) 2.0% MF15

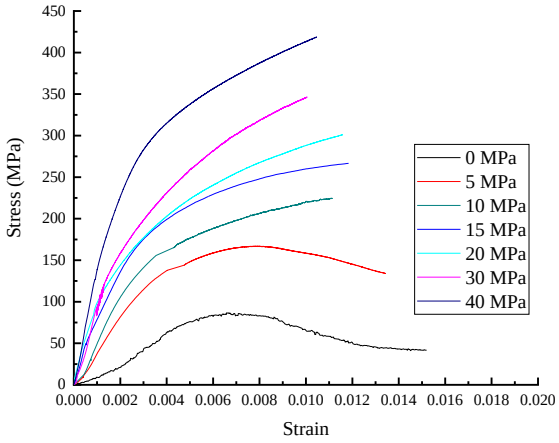

(**d**) 2.5% MF06

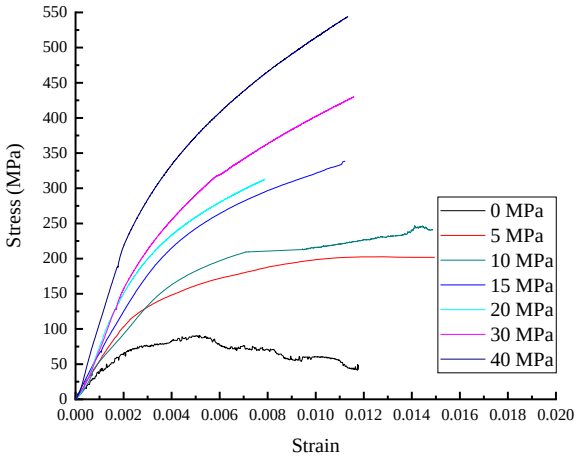

(**e**) 2.5% MF10

Figure 10. Stress–strain curves of SFRGPC specimens under different confining pressures.

Table 3. Triaxial compression test results.

Steel Fiber	V_f (%)	Confining Pressure (MPa)	Strength (MPa)	Peak Strain	Steel Fiber	V_f (%)	Confining Pressure (MPa)	Strength (MPa)	Peak Strain
Without steel fiber	0	0	68.33	0.0025	MF06	2.5	0	82.96	0.0040
		5	125.0	0.0055			5	166.32	0.0085
		10	146.87	0.0081			10	226.17	0.0101
		15	184.77	0.0145			15	264.20	0.0116
		20	222.39	---			20	293.28	---
		30	271.46	---			30	330.17	---
		40	323.75	---			40	390.33	---
MF15	1.0	0	78.63	0.0035	MF10	2.5	0	87.32	0.0052
		5	153.45	0.0058			5	197.72	0.0145
		10	192.11	0.0082			10	243.08	0.0147
		15	261.73	---			15	312.96	---
		20	320.46	---			20	340.79	---
		30	353.44	---			30	423.97	---
		40	398.99	---			40	530.34	---
MF15	2.0	0	83.95	0.0039					
		5	158.47	0.0063					
		10	207.63	0.0084					
		15	256.59	0.0100					
		20	301.03	---					
		30	327.59	---					
		40	403.34	---					

3.3. Failure Criterion

The peak stress increases linearly with the confining pressure, according to the Mohr–Coulomb failure criterion, expressed as

$$\frac{\sigma_1}{f_c} = a + k\frac{\sigma_3}{f_c} \tag{1}$$

where σ_1 is the peak stress, f_c is the uniaxial compression strength, a and k are the empirical coefficients fitted according to the experimental data related to the concrete material, and σ_3 is the confining pressure. The data from the above table are input into the formula, and the results are depicted in Figure 11a. The linear variation does not adequately explain the increase in peak SFRGPC stress with confining pressure, as shown in the graph. Therefore, the Mohr–Coulomb failure criterion (Formula (1)) is rewritten as an exponential function:

$$\frac{\sigma_1}{f_c} = 1 + k\left(\frac{\sigma_3}{f_c}\right)^a \tag{2}$$

where k and a are empirical coefficients.

As shown in Figure 11b and Formulas (3)–(7), as compared to the linear relationship previously proposed, this exponential function can more accurately predict the peak stress of SFRGPC under various confining pressures, steel fiber types, and steel fiber contents. The empirical coefficients k and a are affected by confining pressure and uniaxial compressive strength. This function can be used to predict the triaxial strength through confining pressure and uniaxial compressive strength in subsequent studies, which provides a certain basis for structural design.

$$\text{No Fiber} \quad \frac{\sigma_1}{f_c} = 1 + 5.686\left(\frac{\sigma_3}{f_c}\right)^{0.782} \quad R^2 = 0.99 \tag{3}$$

$$\text{1.0\% MF15} \quad \frac{\sigma_1}{f_c} = 1 + 6.570\left(\frac{\sigma_3}{f_c}\right)^{0.653} \quad R^2 = 0.95 \tag{4}$$

$$2.0\%\ \text{MF15}\quad \frac{\sigma_1}{f_c} = 1 + 6.072\left(\frac{\sigma_3}{f_c}\right)^{0.650} \quad R^2 = 0.98 \tag{5}$$

$$2.5\%\ \text{MF06}\quad \frac{\sigma_1}{f_c} = 1 + 5.548\left(\frac{\sigma_3}{f_c}\right)^{0.569} \quad R^2 = 0.99 \tag{6}$$

$$2.5\%\ \text{MF10}\quad \frac{\sigma_1}{f_c} = 1 + 8.571\left(\frac{\sigma_3}{f_c}\right)^{0.708} \quad R^2 = 0.99 \tag{7}$$

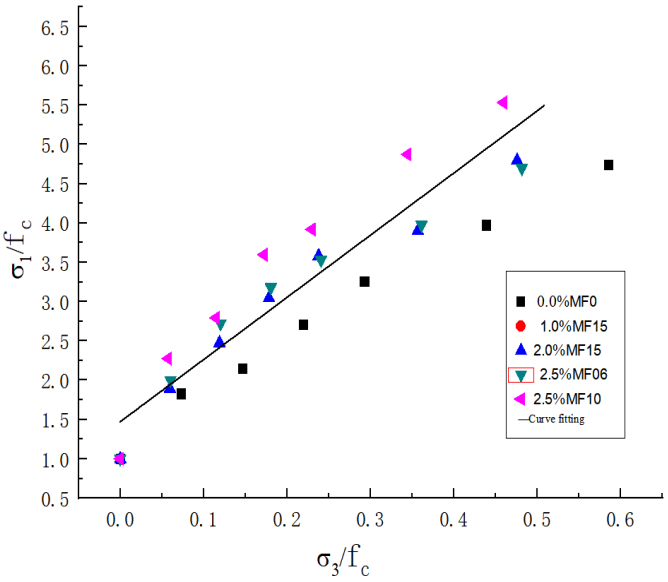

(**a**) Mohr–Coulomb failure criterion

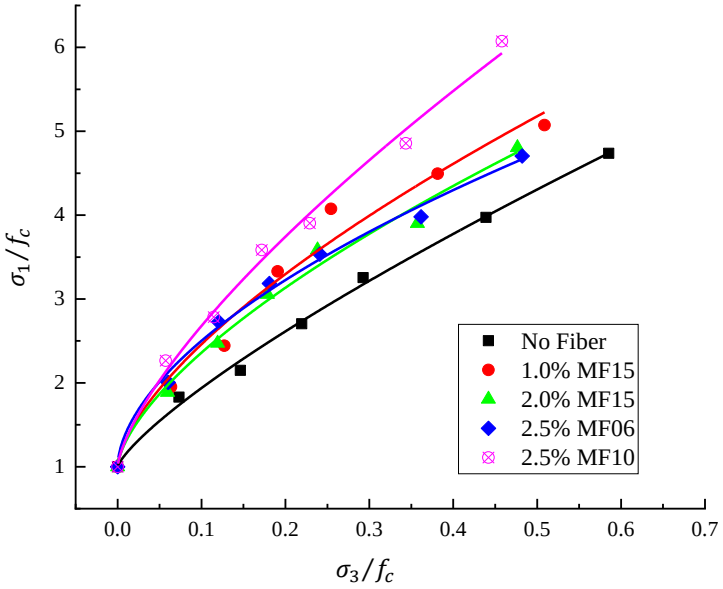

(**b**) Improved Mohr–Coulomb failure criterion

Figure 11. Comparison of peak stress fit and experimental values.

4. Discussion

4.1. Failure Pattern

The SFRGPC specimens' mode of failure can be determined by comparing steel fibers of the same 15 mm length and respective contents of 1% and 2% (Figures 6 and 7). The failure mode of the specimen was affected by the length of the steel fiber and steel fiber content. In this instance, all specimens were longitudinally fractured and damaged, and

the failure behaviors did not vary significantly. The direction of the oblique fracture was 60 to 70 degrees relative to the horizontal. As the confining pressure rose, the damage patterns became oblique rupture failures, and the angle of crack development tended to decrease marginally. Although the specimens' failure mode changed to oblique shear failure as the confining pressure increased, the shear angle (i.e., the angle between the oblique crack and the horizontal plane) of the specimen with a 2.0% steel fiber content was smaller than that with a 1.0% steel fiber content. When the confining pressure exceeded 20 MPa, no surface cracks were evident on the specimen containing 2.0% steel fibers, whereas the specimen containing 1.0% steel fibers displayed obvious oblique shear cracks. Within a given volume, the more added steel fiber, the more energy the specimens can assimilate and the greater their ductility. The test results indicate that a 2% steel fiber content is optimal.

Comparing the failure patterns of specimens S1 and S2 under uniaxial compression (Figures 8 and 9) reveals that both specimens failed in a similar manner, with multiple irregular diagonal fractures. As the confining pressure increased, the specimen's failure pattern changed to oblique shear failure, but specimen S2 had a smaller shear angle than specimen S1. When the confining pressure exceeded 10 MPa, specimen S2 was not damaged, its length shortened, its diameter expanded, and its resistance to damage was greater than that of specimen S1, which continued to develop diagonal cracks.

4.2. Peak Stress

Under varied confining pressures, the trend of the stress–strain curve is evidently distinct, as shown in Figure 10. As the stress increased under uniaxial load, the strain changed swiftly, and the resulting stress–strain curve is steep with distinct peaks. When confining pressure was applied, as the tension gradually increased, the strain was more gradual with no prominent peak point. The section of the curve that consists of a straight line is shorter, whereas the ascending section is longer. The descending portion of the curve decreases more slowly, indicating greater ductility, and the specimen's failure is relatively prolonged. This demonstrates that, under confining pressure, internal fracture and radial deformation of the specimen are constrained, resulting in a gradual increase in concrete strain. The contours still have a descending section when the confining pressure is less than 15 MPa. At confining pressures greater than 15 MPa, the tension and strain continued to increase, with no descending section. In addition, the confining pressure increased the elastic modulus, peak stress, peak strain, and area covered by the stress–strain curve. The results indicate that confinement pressure can drastically alter the brittle failure of SFRGPC.

At a confining pressure, the principal compressive stress and axial strain both increase proportionally with the increase in fiber content, and the curve trend is roughly the same. However, the stress–strain curves of S4 are more extensive than those of S3, demonstrating that steel fiber has a constraining effect on the specimen, inhibiting lateral deformation. With a constant confining pressure and steel fiber content, as the length of the steel fiber increases, the peak strain and peak tension of the specimen also increase.

The steel fiber content and ratio of length to diameter have obvious influence on the compressive strength of SFRGPC. As the steel fiber content increased, the compressive strength increased by 1.15–1.44 times; as the ratio of length to diameter increased, the compressive strength increased by 1.21–1.70 times. The increase in confining pressure can improve the compressive strength of concrete. With the increase in confining pressure, the increase trend of compressive strength becomes smooth.

4.3. Compression Toughness

The area under the stress–strain curve is an index commonly used to determine the compressive toughness of concrete materials [33]. Figure 12 illustrates the definition of the compressive toughness index. In the ascending portion of the stress–strain curve, the critical stress is defined as 85% of the maximal stress at point A. Point B represents the critical strain corresponding to the critical stress. On the strain coordinate axis, points D

and F correspond to strains C and E, respectively, on the stress–strain curve. The indices of compressive toughness, η_{c2} and η_{c3}, can then be defined as follows:

$$\eta_{c2} = \frac{S_{OACD}}{S_{OAB}} \tag{8}$$

$$\eta_{c3} = \frac{S_{OAEF}}{S_{OAB}} \tag{9}$$

where S_{OAB}, S_{OACD}, and S_{OAEF} represent the respective areas enclosed by curves OAB, OACD, and OAEF.

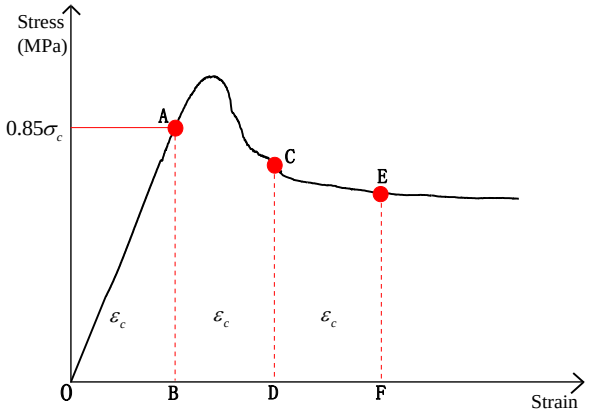

Figure 12. Schematic diagram defining the compressive toughness index.

As shown in Figure 10, when the confining pressure exceeds 10 MPa, the stress increases slowly and does not appear to decrease as the strain increases. Therefore, Table 4 contains compressive toughness index data for only three confining pressures: 0, 5, and 10 MPa.

Table 4. Specimens' compression toughness indices.

V_f (%)	Fiber Length (mm)	Confining Pressure (MPa)	σ_c (MPa)	Critical Stress (MPa)	Critical Strain	S_{OAB}	η_{c2}	η_{c3}
0	0	0	68.47	58.20	0.0020	0.0539	2.56	2.78
		5	117.10	99.45	0.0031	0.152	3.30	5.34
		10	143.85	122.27	0.0036	0.249	2.96	4.98
1.0	15	0	83.31	70.81	0.00278	0.0904	2.52	3.35
		5	149.94	127.45	0.00371	0.187	2.91	4.51
		10	188.16	159.93	0.00372	0.339	2.95	5.22
2.0	15	0	81.57	69.33	0.00283	0.108	2.81	3.15
		5	158.95	135.11	0.0035	0.257	3.63	6.04
		10	202.95	172.50	0.0059	0.481	3.39	5.79
2.5	6	0	86.71	73.70	0.0026	0.084	---	---
		5	164.69	139.98	0.0043	0.374	2.81	4.63
		10	226.30	192.35	0.0054	0.597	2.96	4.99
2.5	10	0	83.86	71.28	0.0037	0.157	2.51	3.36
		5	202.58	172.19	0.0060	0.689	2.712	4.43
		10	255.20	216.92	0.0086	1.117	2.88	4.84

With various steel fiber contents, ratio of length to diameter, and confining pressure conditions, the critical compressive toughness of SFRGPC varies significantly, as shown in Figure 13. The relationship between the confining pressure and the essential compressive toughness exhibits a linear growth pattern. As shown in Table 4, the distinction between compression and compressive toughness index is more intuitive. Consequently, the com-

pressive toughness index can better capture the influence of confining pressure, steel fiber length, and steel fiber content on the compressive toughness of SFRGPC specimens.

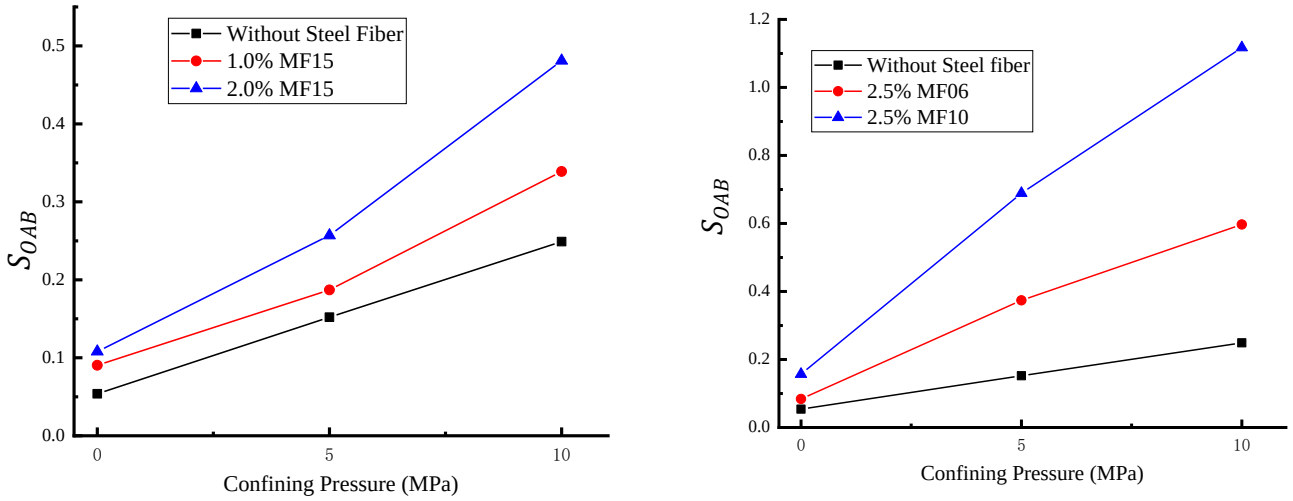

(**a**) Different steel fiber volumes (**b**) Different steel fiber types

Figure 13. S_{OAB}—confining pressure relationship curve.

As depicted in Figure 14a, η_{c3} increases linearly with confining pressure; however, once the confining pressure reaches a certain strength, η_{c3} does not increase significantly and tends to be stable.

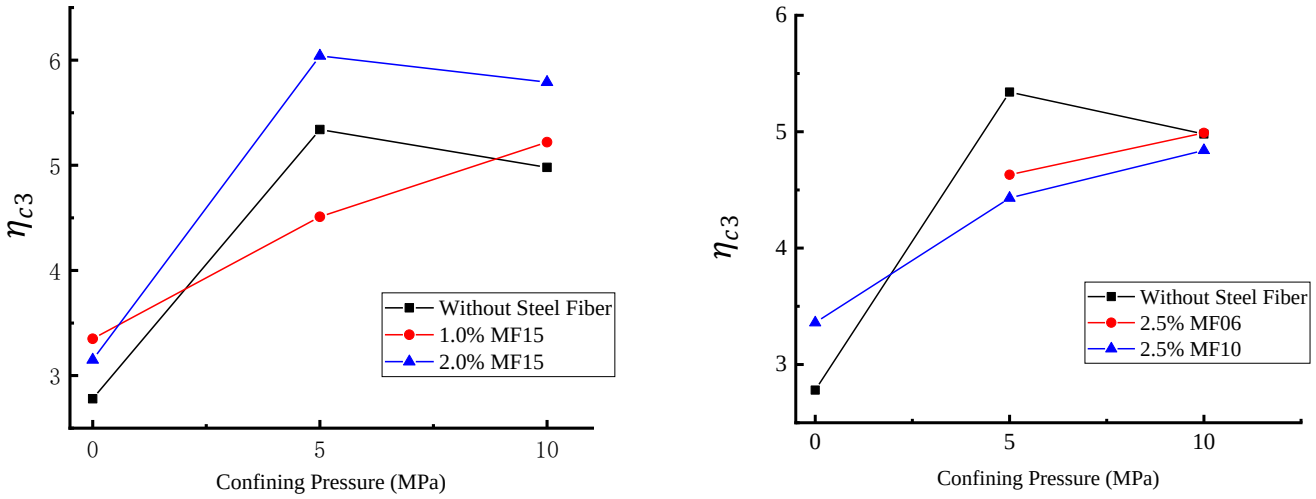

(**a**) Different steel fiber volumes (**b**) Different steel fiber types

Figure 14. η_{c3}—confining pressure relationship curve.

As depicted in Figure 14b, under the same confining pressure condition, a decrease in η_{c3} is not apparent as the steel fiber content increases, indicating a nonlinear decrease. In the process of concrete pouring, due to the agglomeration effect of steel fiber added, the compactness of SFRGPC will be reduced and small bubbles will be produced compared with GPC. In the course of the test, due to the reason of compactness, the stress–strain curve will change to a certain extent, resulting in obvious and unclear compressive toughness changes.

5. Numerical Simulation

5.1. Modeling Method and Verification

The finite element modeling approach utilized in this investigation was validated and verified through the development of numerical models of SFRGPC specimens subjected to

triaxial stress. The results of the tests are compared to determine if the specified material properties, contact method, element size, and method of applying load were accurate.

In this study, the SFRGPC is modeled using the CONCRETE_DAMAGE_Rel3 (MAT_072R3) solid element and material model in LS-DYNA. The MAT_072R3 model is a plastic damage model that depicts the strength development and damage evolution of concrete through three independent strength surfaces: yield strength surface F_y, maximum strength surface F_m, and residual strength surface F_r. In addition, users can also define their own strain rate–dynamic increase coefficient curves and equations of state [34,35].

This investigation used a hexahedral solid element with eight nodes to model concrete, and mesh refinement experiments were conducted. The initial mesh size of concrete was estimated to be 5 × 5 × 5 mm. Once the load–deformation behavior simulated with this mesh size was deemed acceptable, the mesh was refined to 2.5 × 2.5 × 2.5 mm and 1 × 1 × 1 mm. The numerical convergence study indicates that the data of mesh sizes of 2.5 and 1 mm are closer to the experimental curve, and the average difference between the simulation results of two different mesh sizes is less than 2%, as shown in Figure 15. However, the calculation time for the 1 mm mesh was significantly longer. Consequently, the 2.5 mm mesh size was utilized for further analysis and parameterization.

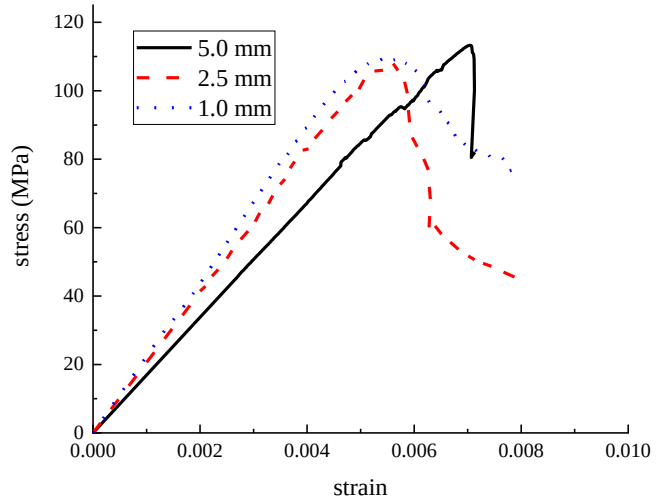

Figure 15. Results of mesh size convergence study.

The user can also automatically generate model parameters that can be checked and modified. Table 5 outlines the parameter values used in this study.

Table 5. Key parameters of CONCRETE_DAMAGE_Rel3 (MAT_072R3) model for SFRGPC.

Density (kg/m^3)	Poisson's Ratio	$f_c^{'}$ (MPa)	f_t (MPa)	b_1	b_2	b_3	Omega
2400	0.19	87	5.45	0.85	2.89	1.88	0.75

The findings of the experiments and simulations of SFRGPC specimens subjected to triaxial strain are shown in Figures 16 and 17, respectively. The transverse fractures created in the numerical model accurately represent the failure mechanism when subjected to triaxial force. The connections between the stress and strain occurring in SFRGPC specimens are shown graphically in Figure 17. The patterns of growth and the location of the curve's inflection point when subjected to triaxial pressures are virtually the same in both the computational results and the experimental data.

Therefore, the numerical model can accurately represent the failure mode and stress–strain curves of SFRGPC specimens subjected to triaxial stresses, confirming the model's dependability.

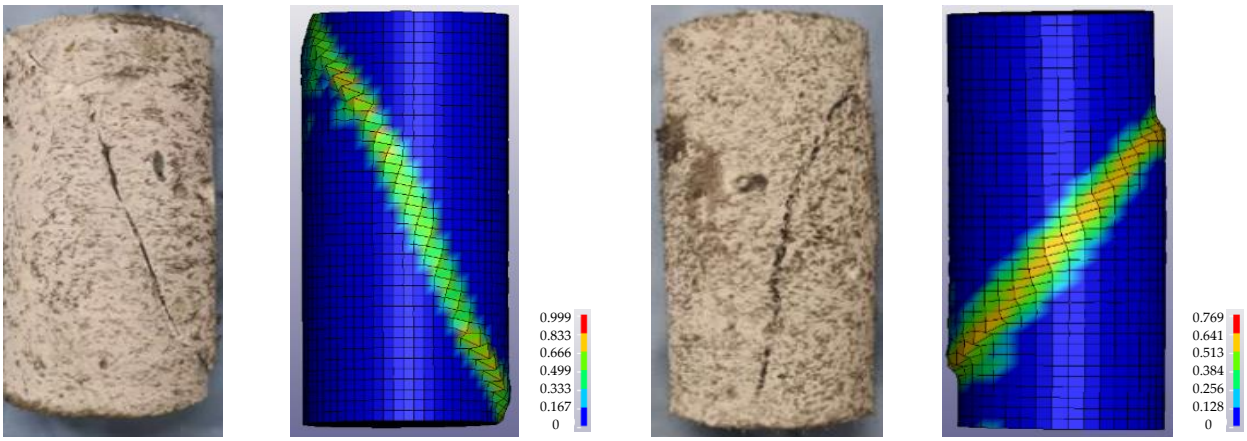

(**a**) 1.0% MF15 (**b**) 2.0% MF15

Figure 16. Effective Plastic Strain of test and simulation results.

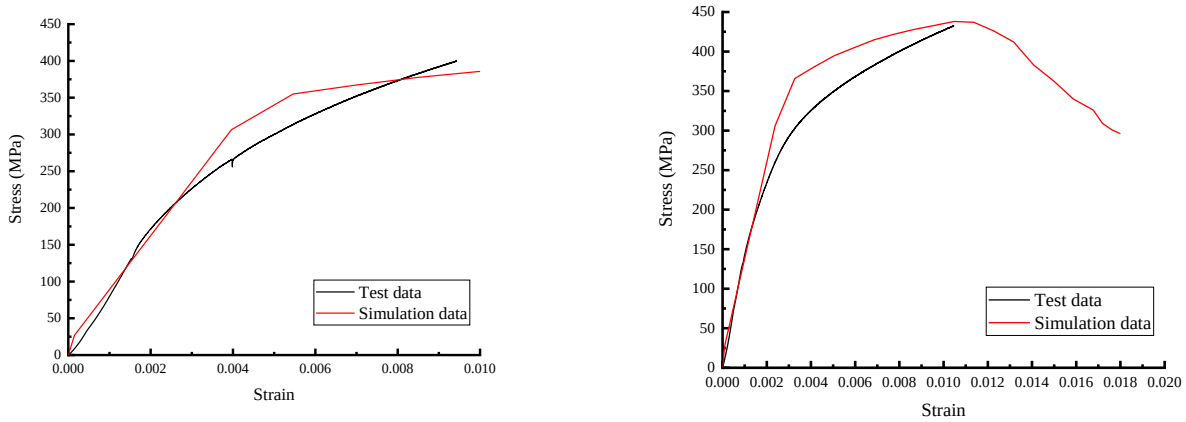

(**a**) 1.0% MF15 (**b**) 2.0% MF15

Figure 17. Comparison of stress–strain curves for experimental tests and simulations.

5.2. Size Effect

5.2.1. Failure Patterns

Figures 18 and 19 illustrate the failure patterns of SFRGPC specimens with varied diameters (50 and 100 mm) and a uniform aspect ratio of 0.5 when subjected to various confining pressures (40, 70, and 110 MPa).

Figure 18 depicts the failure modes of ∅50 × 100 mm SFRGPC specimens with varying steel fiber contents and confining pressures (From blue to red, the damage degree of the specimen is more obvious). As the confining pressure increases, the area of stress clouds expands, and a vertical fracture parallel to the loading direction appears in the middle of the specimen during the early stage of loading, followed by the formation of one or more main cracks that penetrate the specimen. All numerical specimen models subjected to uniaxial compression exhibited excellent ductility. The lower two-thirds of the specimen model incurs substantial damage when the confining pressure exceeds 110 MPa. When the confining pressure is increased, the cylinder gradually expands and extends longitudinally, causing oblique cracking through the existing cracks until failure.

Comparing the failure patterns under 40 and 70 MPa confining pressures, the cracks are progressively distributed throughout the cylinder, not just at the bottom. At a pressure of 110 MPa, the cylinder is damaged, and the longitudinal deformation increases as the circumferential pressure approaches the uniaxial compressive strength.

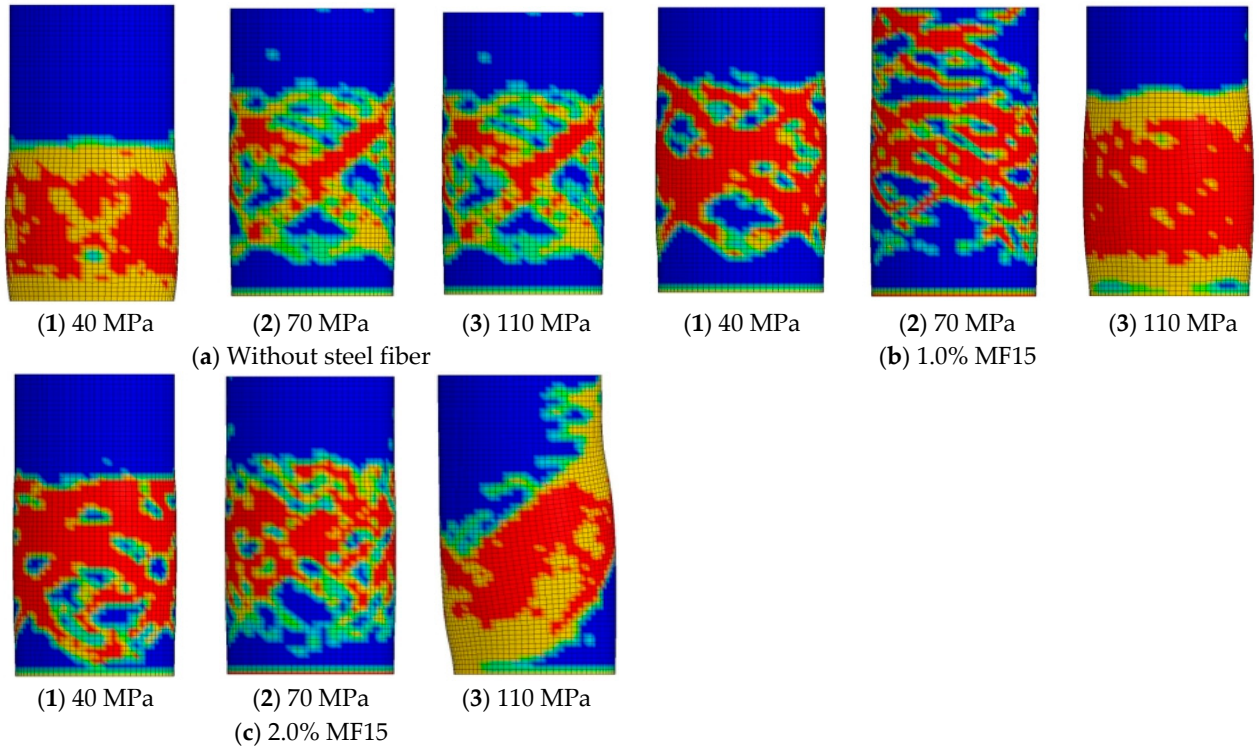

Figure 18. Failure patterns of ∅50 × 100 mm concrete cylinders under different confining pressures.

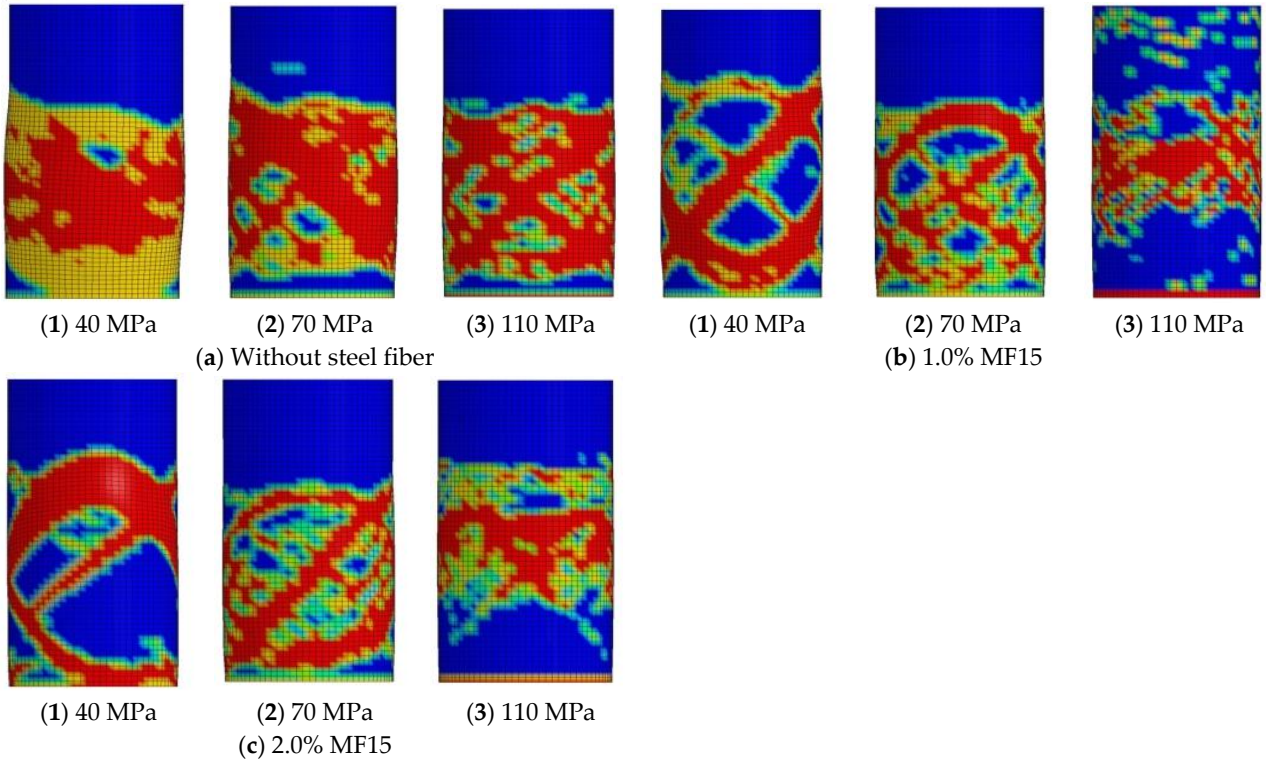

Figure 19. Failure patterns of ∅100 × 200 mm concrete cylinders under different confining pressures.

Figure 19 presents the failure modes of ∅100 × 200 mm SFRGPC models with varying steel fiber contents and confining pressures. As the confining pressure increases, the failure modes become increasingly concentrated at the center for all models, as depicted in the figure. Low confining pressures result in the formation of fractures. With the steel fibers, the SFRGPC cylinders exhibit fewer cracks than GPC without steel fiber. Thus, the steel

fibers improve the ductility of the GPC and allow it to absorb additional energy during the failure process.

In conclusion, when the size of the specimen increases at the same confining pressure, a gradual decrease occurs in the specimen's strength. The damage caused by the failure state of a specimen made of the same material progressively accumulates from deformation to stress and migrates to the specimen's center.

5.2.2. Stress–Strain Curve

As depicted in Figure 20, under the same confining pressure, the concrete cylinder's strength does not significantly decrease as its size increases. The confining pressure restricts its lateral deformation to some degree. With the decrease in stress and peak strain, the deformation reaches its maximum value, and as the volume ratio of steel fiber increases, the internal stress progressively decreases. Although the addition of steel fiber can improve the tensile strength and ductility of SFRGPC, after it exceeds a certain threshold, the effect of size on the specimen's peak tension and peak strain is diminished. Since the modeling is based on the test data, there may be some defects in the production process of the specimen, so the data change significantly in the numerical simulation. In the follow-up study, we will optimize the numerical model and further establish a microscopic model to highlight the strengthening effect of steel fiber.

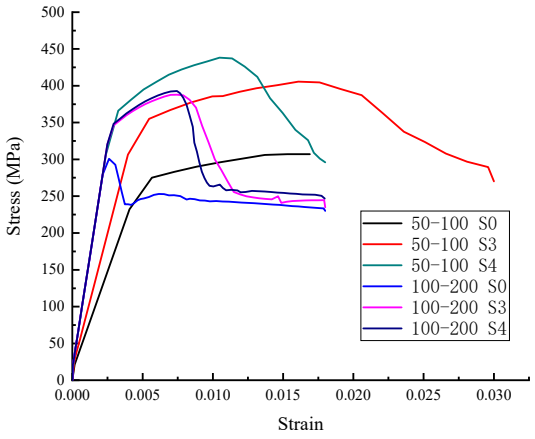

(**a**) 40 MPa

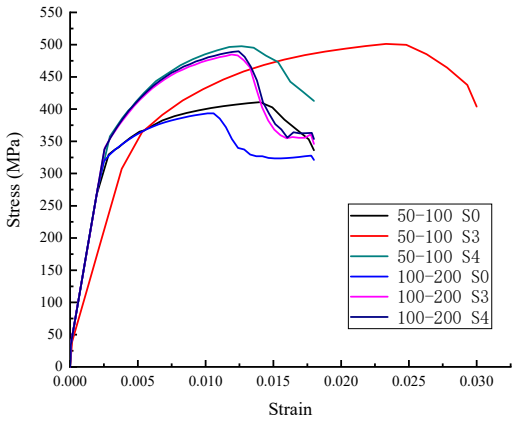

(**b**) 70 MPa

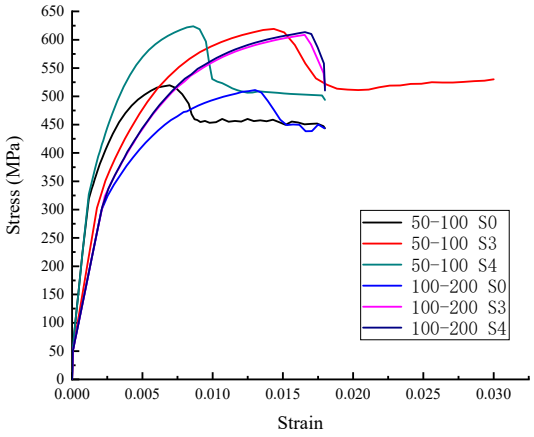

(**c**) 110 MPa

Figure 20. Stress-strain curves of specimens with different sizes and materials under the same confining pressures.

6. Conclusions

This study investigates the relationships of stress, strain, and compressive toughness with confining pressure, steel fiber volume fraction, and steel fiber length in SFRGPC. The material model, generated in LS-DYNA R11.2.2 software, was validated by the test data. The results will better guide the application of SFRGPC in the future application. The key findings are as follows:

1. Under uniaxial compression, with the increase in steel fiber content, the failure mode of the SFRGPC specimens gradually developed into ductile failure.
2. Under multi-axial compression, with the confining pressure increased, a corresponding increase in the angle between the failure crack and the longitudinal axis of the specimens occurred. As the confining pressure and steel fiber content increased, the brittleness of the SFRGPC can be completely eliminated, and its resistance to breaking can be greatly improved.
3. The steel fiber content and ratio of length to diameter have obvious influence on the compressive strength of SFRGPC. As the steel fiber content increased, the compressive strength increased by 1.15–1.44 times; as the ratio of length to diameter increased, the compressive strength increased by 1.21–1.70 times. The increase in confining pressure can improve the compressive strength of concrete. With the increase in confining pressure, the increase trend of compressive strength becomes smooth. The relationship between the peak stress and the confining pressure is linear and proportional.
4. The confining pressure, steel fiber content, and steel fiber length have substantial influences on the compressive toughness index η_{c3}. Under increasing confining pressure, η_{c3} increases linearly; however, after confining pressure is higher than 5 MPa, η_{c3} tends toward a steady state when the confining pressure increases.
5. By modifying the parameters of the material model, a uniform numerical model was established, and the simulation results matched the experimental data.

Author Contributions: Conceptualization, P.W.; methodology, P.W. and Y.Z.; software, X.W. and Y.Z.; validation, P.W.; investigation, Y.Z.; resources, P.W.; data curation, X.W.; writing—original draft preparation, X.W. and Y.Z.; writing—review and editing, P.W.; visualization, Q.L.; supervision, Q.L.; project administration, P.W. All authors have read and agreed to the published version of the manuscript.

Funding: The research presented herein is jointly supported by the National Natural Science Foundation of China (Grant Nos. 52308518 and 52208281) and the Natural Science Foundation of Tianjin, China (Grant No. 23YDTPJC00100).

Data Availability Statement: The data presented in this study are available on request from the corresponding author. The data are not publicly available due to authors need to apply for a patent.

Acknowledgments: The test result was finished in Tianjin Key Laboratory of civil structure protection and reinforcement, Tianjin Chengjian University.

Conflicts of Interest: Author Pengtao Wu was employed by the company Tianjin Building Materials Science Research Academy Co., Ltd. The remaining authors declare that the research was conducted in the absence of any commercial or financial relationships that could be construed as a potential conflict of interest.

References

1. Nguyen, H.T.; Pham, T.K.; Promentilla, M.A.B. Development of Geopolymer-Based Materials from Coal Bottom Ash and Rice Husk Ash with Sodium Silicate Solutions. In Proceedings of the 4th Congrès International de Géotechnique—Ouvrages—Structures, Ho Chi Minh City, Vietnam, 26–27 October 2017; Springer: Singapore, 2017.
2. Mcguire, E.M.; Provis, J.L.; Duxson, P.; Crawford, R.H. Geopolymer Concrete: Is There an Alternative and Viable Technology in the Concrete Sector which Reduces Carbon Emissions. In Proceedings of the Concrete: Building A Sustainable Future, Perth, Australia, 22 October 2011.
3. Davidovits, J. Geopolymer Cement a review. *Geopolymer Sci. Tech.* **2013**, *21*, 1–11.
4. Morsy, M.S.; Alsayed, S.H.; Al-Salloum, Y.; Almusallam, T. Effect of Sodium Silicate to Sodium Hydroxide Ratios on Strength and Microstructure of Fly Ash Geopolymer Binder. *Arab. J. Sci. Eng.* **2014**, *39*, 4333–4339. [CrossRef]

5. Nematollahi, B.; Sanjayan, J. Effect of different superplasticizers and activator combinations on workability and strength of fly ash based geopolymer. *Mater. Des.* **2014**, *57*, 667–672. [CrossRef]
6. Arora, S.; Jangra, P.; Lim, Y.Y.; Pham, T.M. Strength, durability, and microstructure of self-compacting geopolymer concrete produced with copper slag aggregates. *Environ. Sci. Pollut. Res.* **2022**, *30*, 666–684. [CrossRef]
7. Ghafoor, M.T.; Khan, Q.S.; Qazi, A.U.; Sheikh, M.N.; Hadi, M.N.S. Influence of alkaline activators on the mechanical properties of fly ash based geopolymer concrete cured at ambient temperature. *Constr. Build. Mater.* **2021**, *273*, 121752. [CrossRef]
8. Lincy, G.A.; Velkennedy, R. Experimental optimization of metakaolin and nanosilica composite for geopolymer concrete paver blocks. *Struct. Concr.* **2020**, *22*, E442–E451.
9. Yoo, D.Y.; Banthia, N. Mechanical properties of ultra-high-performance fiber-reinforced concrete: A review. *Cem. Concr. Compos.* **2016**, *73*, 267–280. [CrossRef]
10. Ranjbar, N.; Zhang, M. Fiber reinforced geopolymer composites: A review. *Cem. Concr. Compos.* **2019**, *107*, 103498. [CrossRef]
11. Ganesh, A.C.; Muthukannan, M. Development of high performance sustainable optimized fiber reinforced geopolymer concrete and prediction of compressive strength. *J. Clean. Prod.* **2020**, *282*, 124543. [CrossRef]
12. Moradikhou, A.B.; Esparham, A.; Avanaki, M.J. Physical & mechanical properties of fiber reinforced metakaolin-based geopolymer concrete. *Constr. Build. Mater.* **2020**, *251*, 118965.
13. Liu, J.; Wu, C.; Liu, Z.; Li, J.; Xu, S.; Liu, K.; Su, Y.; Chen, G. Investigations on the response of ceramic ball aggregated and steel fibre reinforced geopolymer-based ultra-high performance concrete (G-UHPC) to projectile penetration. *Compos. Struct.* **2021**, *255*, 112983. [CrossRef]
14. Noushini, A.; Hastings, M.; Castel, A.; Aslani, F. Mechanical and flexural performance of synthetic fibre reinforced geopolymer concrete. *Constr. Build. Mater.* **2018**, *186*, 454–475. [CrossRef]
15. Liu, Y.; Zhang, Z.; Shi, C.; Zhu, D.; Li, N.; Deng, Y. Development of ultra-high performance geopolymer concrete (UHPGC): Influence of steel fiber on mechanical properties. *Cem. Concr. Compos.* **2020**, *112*, 103670. [CrossRef]
16. Sharma, U.; Gupta, N.; Bahrami, A.; Özkılıç, Y.O.; Verma, M.; Berwal, P.; Althaqafi, E.; Khan, M.A.; Islam, S. Behavior of Fibers in Geopolymer Concrete: A Comprehensive Review. *Buildings* **2024**, *14*, 136. [CrossRef]
17. Meskhi, B.; Beskopylny, A.N.; Stel'makh, S.A.; Shcherban', E.M.; Mailyan, L.R.; Shilov, A.A.; El'shaeva, D.; Shilova, K.; Karalar, M.; Aksoylu, C.; et al. Analytical Review of Geopolymer Concrete: Retrospective and Current Issues. *Materials* **2023**, *16*, 3792. [CrossRef]
18. Çelik, A.İ.; Özkılıç, Y.O.; Bahrami, A.; Hakeem, I.Y. Effects of glass fiber on recycled fly ash and basalt powder based geopolymer concrete. *Case Stud. Constr. Mater.* **2023**, *19*, e02659. [CrossRef]
19. Özkılıç, Y.O.; Çelik, A.İ.; Tunç, U.; Karalar, M.; Deifalla, A.; Alomayri, T.; Althoey, F. The use of crushed recycled glass for alkali activated fly ash based geopolymer concrete and prediction of its capacity. *J. Mater. Res. Technol.* **2023**, *24*, 8267–8281. [CrossRef]
20. Kufper, H. Behavior of Concrete under Biaxial Stresses. *Aci J.* **1969**, *66*, 656–666.
21. Zhou, J.; Pan, J.; Ma, H.; Zhao, J.; Li, Z. Behavior of high-performance concrete under multiaxial tensile-compressive loading. *Constr. Build. Mater.* **2020**, *260*, 119887. [CrossRef]
22. Wang, Y.Z.; Wang, Y.B.; Zhao, Y.Z.; Li, G.Q.; Lyu, Y.F.; Li, H. Experimental study on ultra-high performance concrete under triaxial compression. *Constr. Build. Mater.* **2020**, *263*, 120225. [CrossRef]
23. Ren, G.M.; Wu, H.; Fang, Q.; Liu, J.Z.; Gong, Z.M. Triaxial compressive behavior of UHPCC and applications in the projectile impact analyses. *Constr. Build. Mater.* **2016**, *113*, 1–14. [CrossRef]
24. Khan, M.Z.N.; Hao, Y.; Hao, H.; Shaikh, F.U.A.; Liu, K. Mechanical properties of ambient cured high-strength plain and hybrid fiber reinforced geopolymer composites from triaxial compressive tests. *Constr. Build. Mater.* **2018**, *185*, 338–353. [CrossRef]
25. Meng, E.; Yu, Y.; Zhang, X.; Su, Y. Experimental and theoretical research on the mechanical performance of totally recycled concrete under triaxial compression after high temperatures. *Constr. Build. Mater.* **2020**, *261*, 120012. [CrossRef]
26. Zhang, K.; Zhao, L.Y.; Ni, T.; Zhu, Q.Z.; Shen, J.; Fan, Y.H. Experimental investigation and multiscale modeling of reactive powder cement pastes subject to triaxial compressive stresses. *Constr. Build. Mater.* **2019**, *224*, 242–254. [CrossRef]
27. Chern, J.C.; Yang, H.J.; Chen, H.W. Behavior of steel fiber reinforced concrete in multiaxial loading. *Aci Mater. J.* **1993**, *89*, 32–40.
28. Lu, X.; Hsu, C. Behavior of high strength concrete with and without steel fiber reinforcement in triaxial compression. *Cem. Concr. Res.* **2006**, *36*, 1679–1685. [CrossRef]
29. Farnam, Y.; Moosavi, M.; Shekarchi, M.; Babanajad, S.K.; Bagherzadeh, A. Behaviour of Slurry Infiltrated Fibre Concrete (SIFCON) under triaxial compression. *Cem. Concr. Res.* **2010**, *40*, 1571–1581. [CrossRef]
30. Wang, Z.; Zhu, B. Strength and Toughness Characteristic of Steel Fiber Reinforced Concrete in Triaxial Compression. *J. Build. Mater.* **2012**, *15*, 301–305+311.
31. Wang, Z.L.; Zhu, H.H.; Wang, J.G.; Zhu, B. Experimental Study on Macroscopic Mechanical Behavior of SFRC under Triaxial Compression. *Mech. Adv. Mater. Struct.* **2012**, *19*, 653–662. [CrossRef]
32. *The ISRM Suggested Methods for Rock Characterization, Testing and Monitoring: 2007–2014*; International Society for Rock, Echanics, Commission on Testing Methods: Lisbon, Portugal, 2015.
33. Wu, P.; Wu, C.; Liu, Z.; Xu, S.; Li, J.; Li, J. Triaxial strength and failure criterion of ultra-high performance concrete. *Adv. Struct. Eng.* **2022**, *25*, 1893–1906. [CrossRef]

34. Malvar, L.J.; Crawford, J.E.; Wesevich, J.W.; Simons, D. A plasticity concrete material model for DYNA3D. *Int. J. Impact Eng.* **1997**, *19*, 847–873. [CrossRef]
35. Crawford, J.E.; Wu, J.; Choi, H.J.; Magallanes, J.M.; Lan, S. *Use and validation of the release III K&C concrete model in LS-DYNA*; Karagozian & Case: Glendale, CA, USA, 2012.